JOINT INSTITUTE FOR NUCLEAR RESEARCH

Dzhelepov Laboratory of Nuclear Problems

FINAL REPORT ON THE START PROGRAMME

Estimation of background and detector efficiency for antiproton production measurement in AMBER experiment.

Supervisor: Dr. Andrei Gridin

Student: Ramez Hany, Egypt,
Cairo University

Participation Period: 21 September - 8 November,
Summer Session 2025

Dubna, 2025

Abstract

This work focuses on the estimation of background contributions and RICH detector efficiency for the measurement of the antiproton production cross section in the AMBER experiment at CERN. A detailed study of background particle contamination, originating from secondary vertices, was performed. The RICH detector's particle identification efficiency and misidentification probabilities were studied through a comparison of Monte Carlo simulations and real data, leading to a significant correction to reconstruction of the simulated data.

Contents

Chapter 1

Precision cross-section needed for advancing cosmic-ray physics.

Charged particles arriving at the Earth from space with energies above 100 MeV – the so-called cosmic rays (CRs) – have always represented a complementary facility to accelerators to advance the understanding of the Standard Model (SM) of Particle Physics. The latest generation of direct-detection space-based experiments (AMS [1], CALET [2], DAMPE [3], ISS-CREAM [4], and PAMELA [5]) have marked the entrance to a high-precision era for CR physics, reaching the few percent level precision from GeV to hundreds of TeV energies. The related discovery potential for the astroparticle field, but also to address fundamental questions still unanswered by the SM among all the nature of Dark Matter (DM), is undoubted. Currently, the interpretation of these data is unfortunately limited by the precision at which production and nuclear fragmentation cross-sections (XS) are known, i.e., in the 10 to 20% precision at most. High-Energy Physics experiments at accelerators, especially at the CERN, have started to provide such measurements, in some cases even going beyond their original physics goals, building a very successful synergy with theoreticians and experimentalists of the astroparticle community.

The so-called indirect search for a DM particle aims at uncovering excesses of the antimatter particle flux in CRs with respect to the modelled astrophysical background. This secondary background originates from interactions of primary GCRs (i.e., present in sources), mainly p and He nuclei, with the interstellar medium (ISM) made of H (90%) and He (10%). A summary of the needed XS, to precisely constrain the secondary antimatter fluxes and to discriminate a possible DM contribution, is reported in Table 1.1, with the main cases detailed below.

Antiprotons are mainly expected to be of secondary origin, as no primary source is known. A few percent precision measurement of their flux, up to 500 GeV energy values, has been published based on 6.5 years of data collected by the AMS experiment [1]. Based on the current predictions, AMS data are globally consistent with the secondary-only production hypothesis [6] , but a possible excess around 10 GeV cannot be further tested because of modelling uncertainties dominated by XS. Reducing them by exploiting collisions, on both H and He targets, is therefore of pivotal importance.

Particle	**Reaction**	**Measurement**	$\sqrt{s}$	**Needed precision**
$\bar{p}$	$p + p \to \bar{p} + X$	$\sigma_{\rm inv}$	5 to 100 GeV	$< 3\%$
	$p + \mathrm{He} \to \bar{p} + X$			$< 5\%$
	$p + p \to \bar{\Lambda} + X$			$< 10\%$
	$p + \mathrm{He} \to \bar{\Lambda} + X$			$< 10\%$
	$p + p \to \bar{n} + X$			$< 5\%$
	$p + n \to \bar{p} + X$			$< 5\%$
$\bar{d}$	$p + p \to \bar{d} + X$	$\sigma_{\rm inv}/n_{\rm tot}$	5 to 100 GeV	(any data)
	$p + \mathrm{He} \to \bar{d} + X$	$\sigma_{\rm inv}/n_{\rm tot}$	5 to 100 GeV	(any data)
	$\bar{p} + p \to \bar{d} + X$	$\sigma_{\rm inv}$	2 to 10 GeV	(any data)
$\overline{\mathrm{He}}$	$p + p \to \overline{\mathrm{He}} + X$	$\sigma_{\rm inv}/n_{\rm tot}$	5 to 100 GeV	(any data)
$e^{\pm}$	$p + \mathrm{He} \to \pi^{\pm} + X$	$\sigma_{\rm inv}$	5 to 100 GeV	$< 5\%$
	$p + \mathrm{He} \to K^{\pm} + X$			$< 5\%$
γ	$p + p \to \pi^0 + X$	$\sigma_{\rm inv}$	5 to 1000 GeV	$< 5\%$
	$p + \mathrm{He} \to \pi^0 + X$			$< 5\%$

Table 1.1: Summary of the wish list of XS, for CRs that can be indirect probes of particle DM. Here, $n_{\rm tot}$ is the integrated multiplicity. The most pressing need is for $\bar{p}$, whose interpretation is already limited by XS uncertainties, but forthcoming data for d and possible He events from AMS call for new XS measurements as well. Table taken from [**?**].

Chapter 2

AMBER experiment setup

The AMBER experiment at the M2 secondary beam line of CERN SPS is a fixed-target experiment that started data-taking in 2023, as the successor of the long-standing COMPASS experiment. Within the first approved phase of the experiment from 2023 to around 2031, AMBER reused and upgraded the 2-stage magnetic spectrometer from COMPASS. The experimental setup includes two differential Cherenkov counters (CEDARs), with achromatic ring focus to identify protons in the mixed hadron beam, a cryogenic target filled with the He gas, and the AMBER spectrometer to characterise the particles created in the interaction. In order to measure their momentum, the AMBER spectrometer consists of around 300 tracking detector planes and two spectrometer magnets, with a bending strength of up to 1 Tm and 4 Tm, respectively. Additionally, a RICH detector and muon detectors allow particle identification over an extensive momentum range. Antiprotons with a total momentum between 10 GeV/c and 60 GeV/c, and transverse momentum up to 2 GeV/c, are identified. In 2023, a cryogenic target filled with He was used to acquire data aiming to a $\bar{p}$ production measurement in pHe collisions $p + {}^4\text{He} \to \bar{p} + X$. Data were recorded at six different collision energies between $\sqrt{s_{\text{NN}}} = 10.7$ GeV and $\sqrt{s_{\text{NN}}} = 21.7$ GeV. In 2024, a new cryogenic target was built to allow the usage of flammable gases, such as H and D. For both targets, collisions at 12.3 GeV, 17.3 GeV, and 21.7 GeV were recorded, with an identical spectrometer setup.

For the purpose of the antiproton production cross section, the beam line was set to hadron configuration at an intensity of roughly 10^5 p/spill. At the SPS, one spill corresponds to a delivery of particles lasting ~ 5 seconds. Typically during the 2023 run we had a supercycle of 2 spills every ~ 30 seconds. This intensity has been chosen in order to prevent a high DAQ dead time and to avoid the pre-scaling of the trigger rate. The hadron beam composition is reported in Table 2.1.

The data handling and processing for the 2023 AMBER run relied on a the software infrastructure inherited and maintained from the COMPASS experiment. Monte Carlo simulated events were first generated using PYTHIA8, then passed through TGEANT, a GEANT4-based framework customized for the spectrometer that simulated the full detector geometry and response. The resulting data were subsequently reconstructed and analyzed within the COMPASS Reconstruction and Analysis software (CORAL), ensuring a consistent treatment of both Monte Carlo and real datasets. The reconstructed

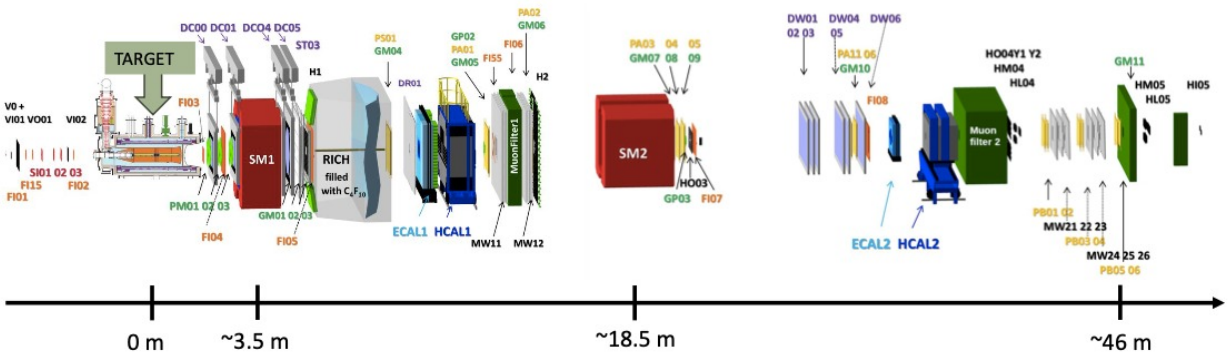

Figure 2.1: AMBER Spectrometer.

Beam mom.	Positive beams			Negative beams		
[GeV/c]	π^+	K^+	p	π^-	K^-	$\bar{p}$
100	0.618	0.015	0.367	0.958	0.018	0.024
160	0.360	0.017	0.623	0.966	0.023	0.011
190	0.240	0.014	0.746	0.968	0.024	0.008
200	0.205	0.012	0.783	0.969	0.024	0.007

Table 2.1: The hadron beam composition at different momenta at the M2 beam line [8, 9]

output from both data and simulation was stored in a compact Data Summary Tape (DST) format, enabling analysis using the Physics Analysis Tool (PHAST) within the ROOT framework. A schematic overview of the processing chain for both Monte Carlo and real data is presented in Fig. 2.2. It is important to note that the MC simulation now has RICH-1 efficiency. In this work, the analysis was carried out using the PHAST framework for both Monte Carlo and real data processing, while ROOT was employed for visualization and plotting of the resulting distributions. Additionally, PYTHIA8 was used for event generation and for testing specific aspects of the analysis chain.

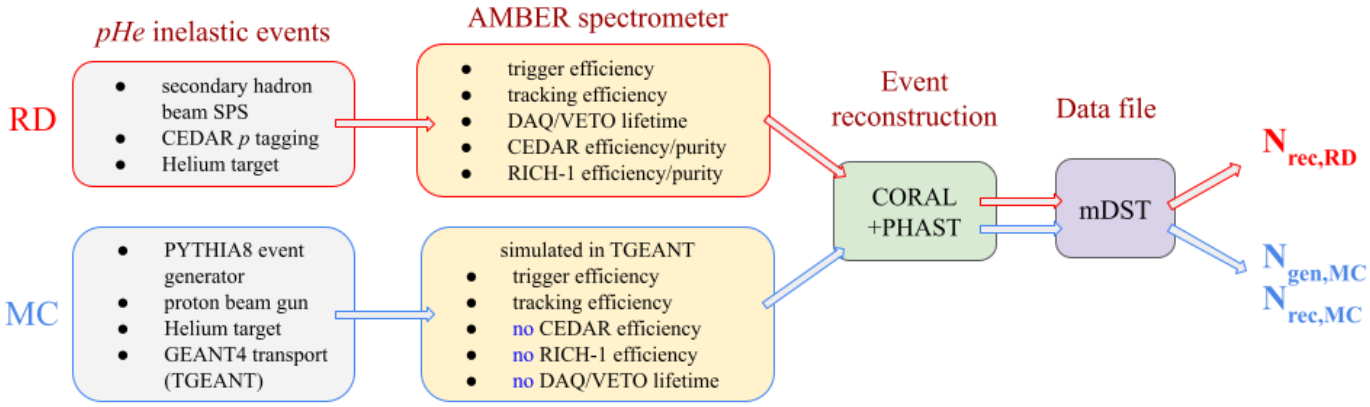

Figure 2.2: Block diagram illustrating the processing workflow for Monte Carlo and real data. The simulation omits CEDAR and RICH-1 efficiency effects, as well as DAQ/VETO deadtime. Figure is from [10]

The cross section of antiprotons is obtained from the number of reconstructed and identified signal events after correcting for background contributions and detector efficiencies. It can be expressed as:

$$\sigma = \frac{N^h_{\text{measured}} - N^h_{Background}}{\mathcal{L} \cdot A \cdot \epsilon_{RICH} \cdot \epsilon_{DAQ} \cdot \epsilon_{VETO}} \tag{2.1}$$

In this analysis particular attention is given to estimating the term $N_{\text{Background}}$, which accounts for events that are incorrectly reconstructed or misidentified as antiprotons, as well as the RICH detector efficiency, ϵ_{RICH}.

Chapter 3

PID Analysis for RICH signal

In the AMBER experiment, the RICH-1 detector utilizes a 3-meter-long vessel filled with a C_4F_{10} gas radiator. Cherenkov photons are focused by a large, segmented mirror wall onto an array of photon detectors, which in AMBER include Multi-Anode Photomultiplier Tubes (MAPMTs) in the central region and gas-based detectors in the periphery. This setup provides efficient identification of hadrons in the momentum range crucial for the experiment's physics program, making it a powerful tool for isolating antiprotons from other particle backgrounds. A significant preparatory step was the removal of the RICH-1 beam pipe to extend the acceptance for very forward-produced particles. The trigger logic was kept minimal-bias, requiring a beam particle signal in coincidence with the absence of hits in downstream beam killers and upstream veto counters, ensuring the selection of inelastic interactions within the helium target.

Cherenkov radiation is an electromagnetic radiation emitted when a charged particle travels through a dielectric medium at a speed greater than the phase velocity of light in that medium.

The key property is the Cherenkov angle (θ_C), given by the relation:

$$\cos\theta_C = \frac{1}{\beta n} \tag{3.1}$$

where n is the refractive index of the medium and $\beta = v/c$ is the particle's speed relative to the speed of light in a vacuum.

Each particle species has a characteristic Cherenkov angle for a given momentum, allowing them to be distinguished. Since $0 < |\cos\theta_C| < 1$ and $\cos\theta_C = \frac{1}{n\beta}$, there is a lower threshold limit for the particle's momentum which is given by:

$$p_{th} = \frac{m}{\sqrt{n^2 - 1}} \tag{3.2}$$

So the range in which a particle can produce signal (Cherenkov photons) is determined by the mass and the refractive index of the medium.

In general, particles are identified by their mass and electrical charge. The mass cannot be measured directly and 2 other quantities must be measured: momentum, kinetic energy and/or velocity. By exploiting the basic relation:

$$m = \frac{p}{c\beta\gamma} \tag{3.3}$$

it is possible to fully identify the particle (β is the ratio v/c and $\gamma = E/mc^2$). Curvature in a static magnetic field leads to the charge sign and the momentum value, while the β factor could be given by several methods: ionization energy loss, time of flight, Cherenkov radiation and transition radiation. The resolution on mass can be calculated by propagating the errors in Eq. 3.3:

$$\left(\frac{dm}{m}\right)^2 = \left(\gamma^2\frac{d\beta}{\beta}\right)^2 + \left(\frac{dp}{p}\right)^2 \tag{3.4}$$

To estimate the mass precisely we need a very good determination of momentum and velocity. If we assume that the determination of the momentum is precise enough, the mass resolution is led by the

accuracy in the determination of the velocity. The differences between the masses of two particles m_1 and m_2 and same momentum p can be expressed as:

$$m_1^2 - m_2^2 = p^2 \frac{2\Delta\beta(\beta_1 + \beta_2)}{c^2(\beta_1 \cdot \beta_2)^2} \tag{3.5}$$

where $\Delta\beta = |\beta_1 - \beta_2|$. Assuming $\beta_1, \beta_2 \sim \beta$:

$$\frac{\Delta\beta}{\beta} = \frac{(m_1^2 - m_2^2) \cdot c^2}{2p^2} \tag{3.6}$$

indicating that the beta resolution becomes important at higher momenta. In AMBER, a beta resolution of the order of 10^{-5} is required for identifying particles in the spectrometer up to 60 GeV/c and of the order of $\sim 10^{-6}$ for beam particles.

The identification of the beam particle is performed by using the CEDAR detectors installed upstream the target. In 2023 at 190 GeV/c, the protons signal is very well separated from pions and kaons and we can obtain an almost pure sample of protons with a tagging efficiency of 96%.

Some of the basic definitions that will be used in this work, like efficiency, contamination and purity, are intrinsic characteristics of any PID device. A wrong identification will fail in identifying the particle A (*inefficiency*) or will classify the particle B as A (*contamination*). The efficiency in the identification of a particle of type A is given by the ratio of the number of particles recognized as type A ($N_{A,\text{identified}}$), divided by the total number of particles of type A ($N_{A,\text{total}}$).

$$\varepsilon_{A\to A} = \frac{N_{A,\text{identified}}}{N_{A,\text{total}}} \tag{3.7}$$

while contamination is given by the ratio of the number of wrongly identified particles, to the total number of particles.

$$\varepsilon_{B\to A} = \sum_{B,B\neq A} \frac{N^B_{A,\text{identified}}}{N_{A,\text{total}}} \tag{4.6}$$

And Purity is the fraction of identified particles that are correctly identified.

$$\text{Purity}_A = \frac{N_{A,\text{identified correctly}}}{N_{A,\text{identified}}} \tag{3.8}$$

The PID relies on an extended maximum likelihood (EML) method. to overcome the case in which many hypotheses are similar, the likelihoods ratio is taken in to account. If this ratio is above a defined value, the identification is positive. Each particle type has a momentum threshold for producing Cherenkov light, according to Eq. 3.2. In the RICH-1 with C_4F_{10} radiator the thresholds are about:

- π 2.5 GeV/c
- K 9 GeV/c
- p 18 GeV/c

The protons emit Cherenkov light only above 18 GeV/c, constraining the phase space covered with active identification above that threshold. There is a region in momentum, however, in which pions and kaons do emit Cherenkov photons, while protons do not. This region is in between the kaon and proton threshold. There, we can use the RICH in so-called "VETO mode" exploiting the high efficiency in pion and kaon identification at those momenta. Two scenarios are possible: a proton may pass without leaving any light and all the likelihoods will be 0, or some photons may be detected and the likelihoods are computed. The phase space for PID is thus divided in two (plus one) regions:

- $p \in [p_{\text{thr},K}, p_{\text{thr},p}]$ GeV/c. Below proton momentum threshold. Active identification for K and π. VETO mode for p

- $p \in [p_{\text{thr},p} - \delta, p_{\text{thr},p} + \delta]$ GeV/c. Overlapping zone. Active identification for π and K. The proton candidates must satisfy the likelihood ratio selection criteria required for both below and above proton momentum threshold.
- $p \in [p_{\text{thr},p}, 60]$ GeV/c. Above proton momentum threshold. Active identification for all particles.

The likelihood ratios cuts are shown in Table 3.1.

3.1 Event selection and cuts

The measured number of hadrons is computed after a selection of inelastic events in the helium target. After the data reconstruction with CORAL, the cuts applied to select the inelastic events from real data are enumerated here:

1. trigger mask has physics trigger bit fired The trigger mask provides a bit map of triggers fired. The trigger required is bit 1, that is our physics trigger, made of the anti-coincidence between a beam trigger and the VETO detectors.
2. TiS is in $[1.2, 5.4]$ s time window. A typical spill lasts ~ 4 seconds. With the physics trigger used in this data taking the event rate is $\sim 10^5 \text{ev}/spill$.
3. multiplicity of CEDAR1 and CEDAR2 is larger than 6 The hadron tagging in the beam is provided by the CEDAR detectors. The required PMTs multiplicity is at least 6 on both CEDARs;
4. primary vertex position is inside the liquid helium target. The final cut is a cylinder parallel to the beam with Z dimension $\subset [-65, 65]$ cm and radius of 3.4 cm.
5. primary vertices with only one outgoing track are excluded;

The track selection follows minimum criteria to ensure a good reconstruction of the hadron candidates. From all the vertex selected in inelastic events, the outgoing tracks passing the following cuts constitute the raw sample of hadrons:

1. $\chi^2/ndf < 10$

   the reduced χ^2 must be smaller than 10 to ensure proper reconstruction;
2. the radiation length crossed is $X/X_0 < 10$

   The radiation length cut is applied to exclude muons from the sample;
3. First and last measured point are respectively before and after SM1

   The first spectrometer is located roughly at 3.50 m after the target. The cut applied is $Z_{\text{first}} <$ 350 cm and $Z_{\text{last}} > 350$ cm;
4. track can be extrapolated to the RICH;
5. track has RICH information;

	$\pi^\pm/\pi^\mp$	$K^\pm/K^\mp$	$p(\bar{p})$	
Momentum range	$p > p_{\pi,thr}$	$p > p_{K,thr}$	$p_{K,thr} < p < p_{p,thr}$	$p > p_{p,thr}$
$LH(\text{i})/LH(\pi)$	-	> 1.06	-	> 1.06
$LH(\text{i})/LH(K)$	> 1.06	-	-	> 1.06
$LH(\text{i})/LH(P)$	> 1.06	> 1.06	-	-
$LH(\text{i})/LH(\text{Bkg})$	> 1.25	> 1.25	-	> 1.25
	-	-	not π or K	-
$LH(\pi)/LH(\text{Bkg})$	-	-	< 2.5	-
$LH(K)/LH(\text{Bkg})$	-	-	< 2.5	-

Table 3.1: LH ratios cuts. From [10]

Hadrons	Channel	BR
K_S	$\pi^+\pi^-$	$(69.20 \pm 0.05)\%$
ϕ	K^+K^-	$(48.9 \pm 0.5)\%$
$\Lambda(\bar{\Lambda})$	$p\pi^-(\bar{p}\pi^+)$	$(63.9 \pm 0.5)\%$

Table 3.2: Summary of the V^0 decay channels used for calibration. Branching ratio (BR) values are from [11].

The MC reconstructed selection follows almost the same criteria of the real data selection. The only differences are related to the bad spills and time in spill selection and to the CEDAR cuts and the RICH likelihood ratios cuts. The hadron species are identified using the MC truth.

3.2 PID Efficiency

The efficiency of PID is all about extracting the identification and misidentification probabilities. These probabilities can be grouped in the so-called RICH-1 PID efficiency matrix:

$$M^{\pm}_{RICH}(p,\theta) = \begin{pmatrix} \epsilon(\pi \to \pi) & \epsilon(K \to \pi) & \epsilon(p \to \pi) \\ \epsilon(\pi \to K) & \epsilon(K \to K) & \epsilon(p \to K) \\ \epsilon(\pi \to p) & \epsilon(K \to p) & \epsilon(p \to p) \end{pmatrix} \tag{3.9}$$

where the diagonal of the sub-matrix gives the probability to correctly identify a particle species and the offdiagonal elements are the misidentification probabilities.

To properly account for detector efficiencies, the particle identification (PID) and misidentification probabilities were extracted directly from real data. AMBER collaboration have used track samples originating from the decays of secondary V^0 vertices (Λ, $\bar{\Lambda}$, K^0_S, and ϕ), as summarized in Table 3.2. The momentum distributions of the decay products from these V^0 particles, generated with PYTHIA8, are presented in Figure 3.1. As clearly shown, the production rates of kaons, protons, and pions are significantly reduced at lower beam energies compared to the 190 GeV data. Consequently, the limited statistics of these decay products at 60 GeV/c do not allow for a reliable determination of the RICH efficiencies using the V^0 method. In this work, the RICH efficiencies were extracted from MC for the first time.

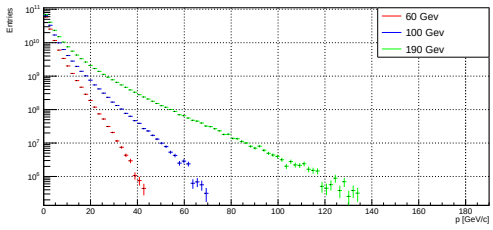

(a) $\pi^{\pm}$ from $K^0_S \to \pi^+\pi^-$

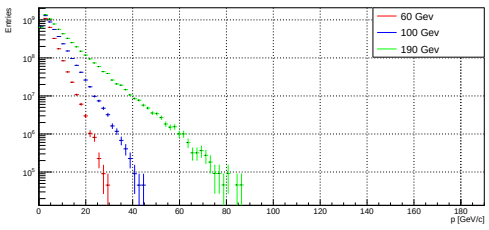

(b) $K^{\pm}$ from $\phi \to K^+K^-$

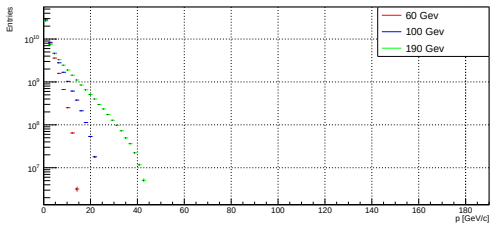

(c) $\pi^{\pm}$ from $\Lambda(\bar{\Lambda}) \to p\pi^-(\bar{p}\pi^+)$

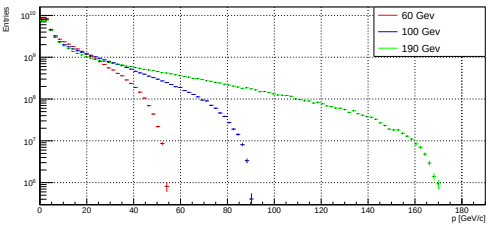

(d) $p(\bar{p})$ from $\Lambda(\bar{\Lambda}) \to p\pi^-(\bar{p}\pi^+)$

Figure 3.1: PYTHIA8 generated momentum distributions of daughter particles from V^0 decays for incident beam energies of 60 GeV (red), 100 GeV (blue), and 190 GeV (green).

Figure 3.2 presents the computed elements of the identification efficiency matrix for negatively charged particles as a function of momentum. The RICH-1 detector shows excellent π identification efficiency (>97%) up to 40 GeV/c. A small misidentification of kaons is observed near their Cherenkov threshold (10–12 GeV/c). Proton identification remains highly efficient above the threshold (>18 GeV/c). These results are in good agreement with the efficiencies extracted from real data using the V^0 method, as shown in Fig. 4.15 of Ref. [10].

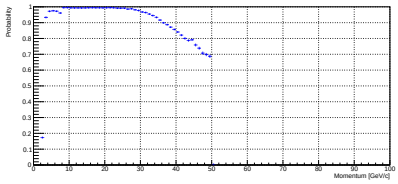

(a) $\epsilon(\pi^- \to \pi^-)$

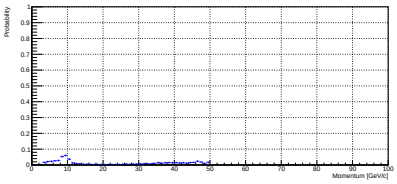

(b) $\epsilon(K^- \to \pi^-)$

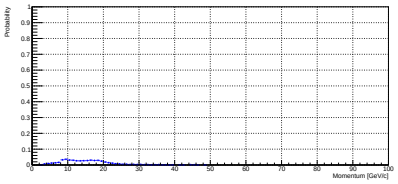

(c) $\epsilon(\bar{p} \to \pi^-)$

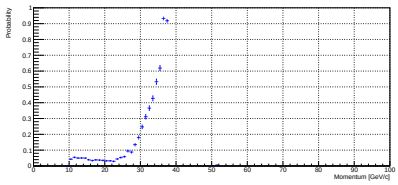

(d) $\epsilon(\pi^- \to K)$

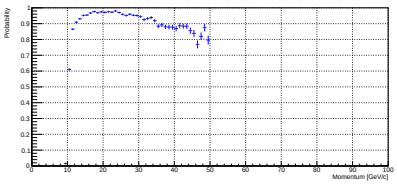

(e) $\epsilon(K^- \to K^-)$

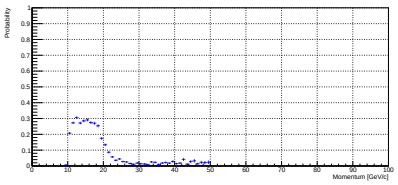

(f) $\epsilon(\bar{p} \to K^-)$

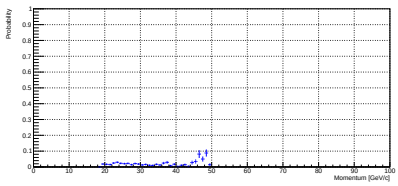

(g) $\epsilon(\pi^- \to \bar{p})$

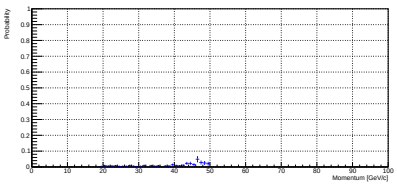

(h) $\epsilon(K^- \to \bar{p})$

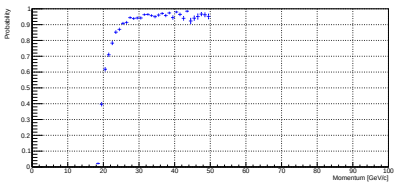

(i) $\epsilon(\bar{p} \to \bar{p})$

Figure 3.2: Probability of misidentification of each element in PID efficiency matrix as a function of momentum.

Chapter 4

MC/RD comparison

Until September 2025, the RICH simulation was not yet implemented or reviewed. Consequently, our MC/RD study faced several challenges:

1. A large number of protons and kaons were observed around 25 GeV/c: An initial discrepancy was identified in the reconstruction of these particles, as illustrated in Fig. 4.1. This issue was traced to an incorrect value of the refractive index used in the reconstruction of MC data. After tuning the refractive index to accurately reproduce the real detector conditions, the problem was resolved, resulting in the clean distributions shown in Fig. 4.2.

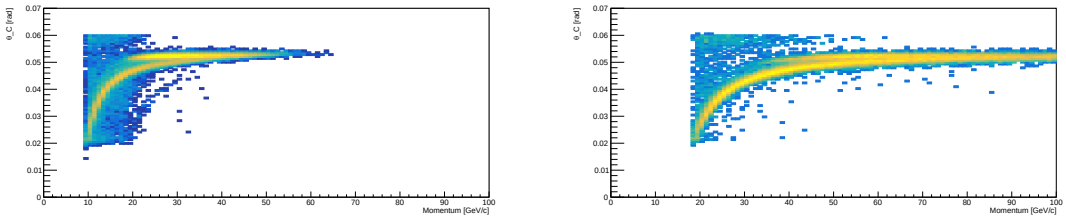

(a) K (b) p

Figure 4.1: MC reconstructed momentum versus Cherenkov angle distribution for kaons and protons before refractive index correction.

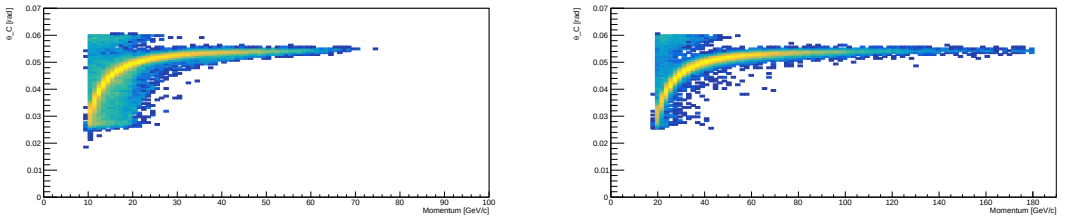

(a) K (b) p

Figure 4.2: MC reconstructed momentum versus Cherenkov angle distribution for kaons and protons after refractive index correction.

2. An excessive number of photons were observed in the reconstructed RICH rings: The peak efficiency is defined as the highest fidelity achieved in reconstructed data, representing the optimal performance region of the detector for a given observable. A comparison of the distributions shown in Fig. 4.3 illustrates the importance of this calibration process: the untuned Monte Carlo (MC) simulation (b) displays a clear mismatch with the real data (a), revealing inherent inaccuracies in the default detector modeling. After applying the appropriate tuning procedures, the resulting tuned MC (c) shows excellent agreement with real data, confirming the validity of the optimized simulation parameters. The improved consistency between simulation and real data is further confirmed by the MC/RD ratios presented in Fig. 4.4.

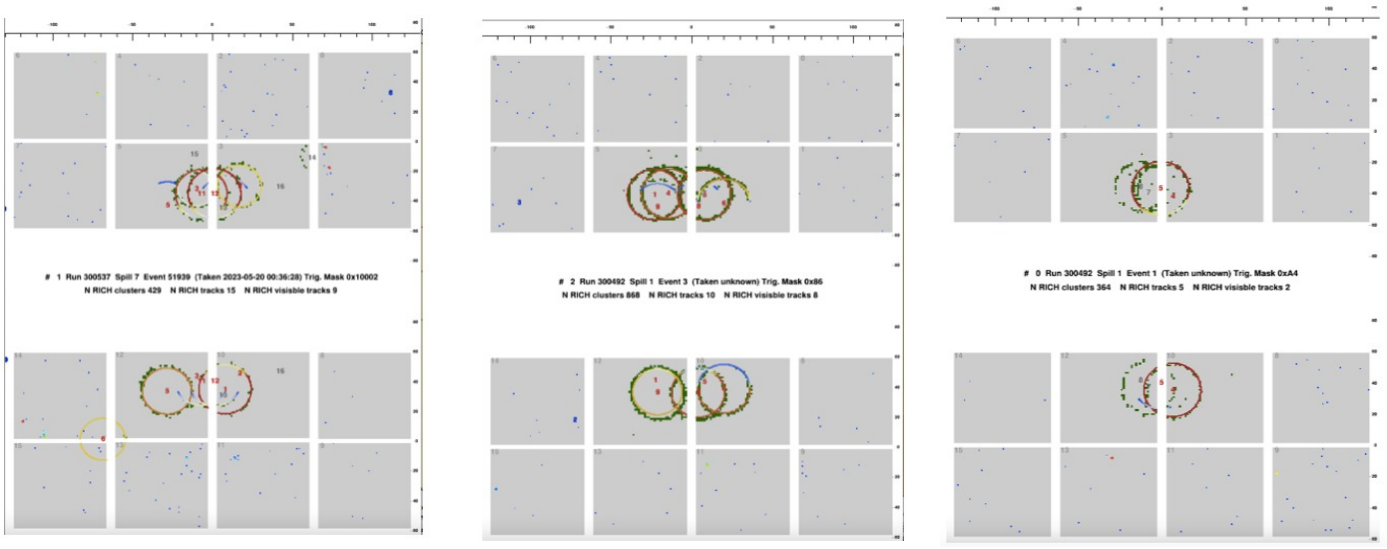

(a) Real Data peak efficiency (b) Untuned MC peak efficiency (c) Tuned MC peak efficiency

Figure 4.3: Evolution of the detector response through different stages of simulation tuning.

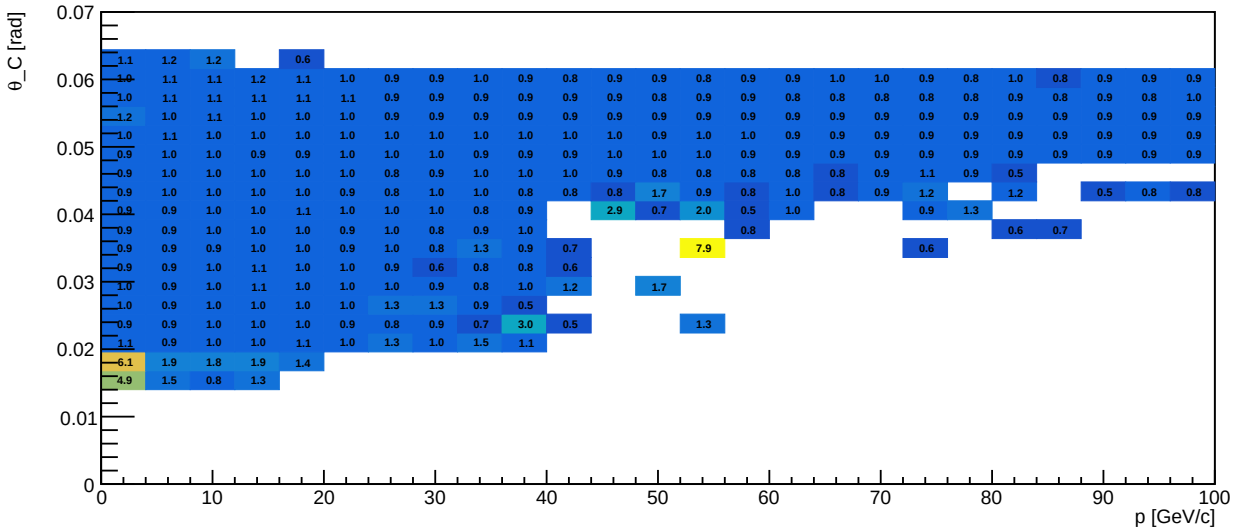

Figure 4.4: 2D MC/RD ratio after final tuning, shows the Cherenkov angle versus momentum, weighted by the number of photons detected in the RICH PMTs, showing good agreement.

3. A low MC/RD ratio was observed for protons and kaons: The results presented in Fig. 4.5 reveal distinct behaviors among different particle species. While pions exhibit a good level of agreement between MC and real data, the MC notably overestimates the yields of kaons and protons. This discrepancy is attributed to the event generation model in PYTHIA8, as the detector efficiencies from MC and RD are found to mostly consistent.

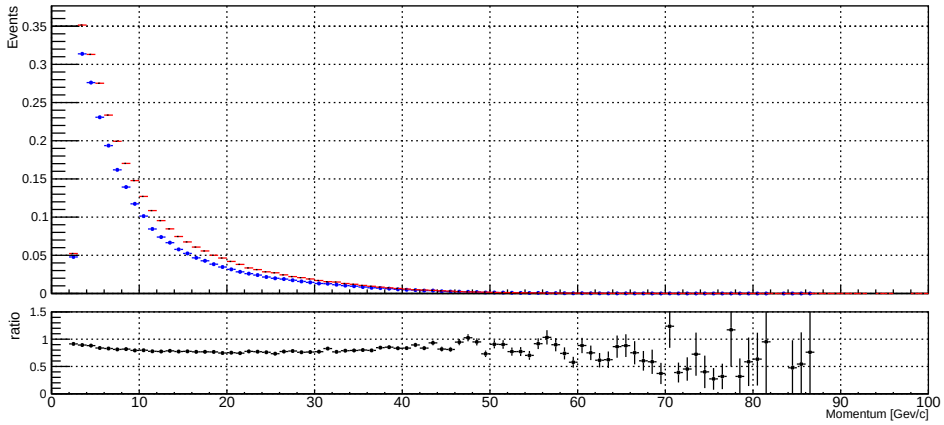

(a) π

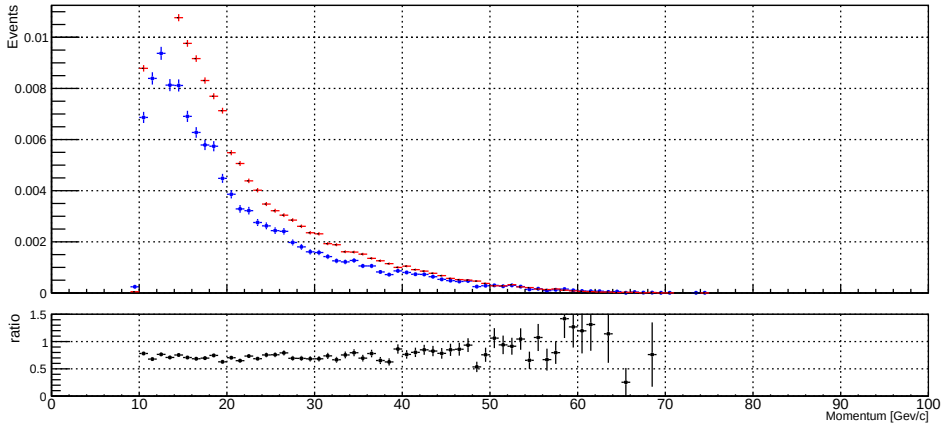

(b) K

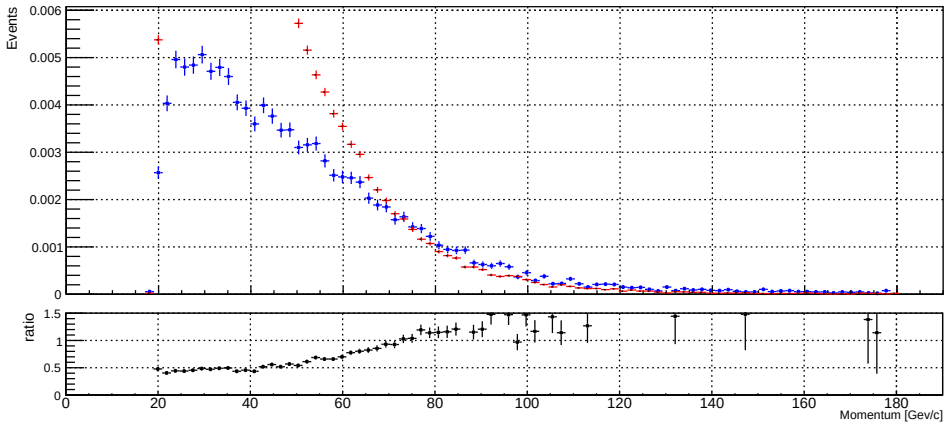

(c) p

Figure 4.5: MC/RD ratio as a function of momentum for pions, kaons, and protons. Real data is in blue, and MC simulation is in red.

Chapter 5

Background Estimation

Background antiprotons are defined as antiprotons arising from secondary vertices that are erroneously reconstructed as primary vertices. Several scenarios can lead to such misreconstruction:

1. Elastic interaction of the beam proton at the primary vertex, with both the primary and secondary vertices located inside the target.

2. Inelastic interaction of the beam proton at the primary vertex, with both vertices inside the target.

3. The beam proton interacts at a primary vertex located outside the target, while the secondary vertex is inside the target.

4. The beam proton interacts at the primary vertex, producing an antiproton outside the target, while the secondary vertex remains inside.

To quantify the level of background contamination in the reconstructed MC sample, a coefficient α is introduced. This coefficient is defined as the ratio of the number of background particles originating from secondary vertices to the total number of reconstructed signal particles:

$$\alpha = \frac{N_{SV}}{N_{PV} + N_{SV}}, \tag{5.1}$$

A smaller value of α indicates a cleaner sample with minimal background contribution, reflecting the effectiveness of vertex reconstruction and selection criteria in distinguishing genuine signal events from background sources. A fully validated MC model allows the assumption that the α coefficient derived from simulation closely represents the one obtained from real data.

For both cases 1 and 2, the background receives contributions from elastic and inelastic MC processes. The corresponding background fractions are defined as

$$\alpha_{\text{el}} = \frac{N^{\text{el}}_{\text{bkg}}}{N^{\text{el}}_{\text{Events}}}, \tag{5.2}$$

$$\alpha_{\text{inel}} = \frac{N^{\text{inel}}_{\text{bkg}}}{N^{\text{inel}}_{\text{Events}}}, \tag{5.3}$$

where N_{Events} is the total number of generated events in each sample, and N_{bkg} is the number of background antiprotons.

The total background fraction is defined as a weighted combination of the elastic and inelastic contributions:

$$\alpha = \frac{\alpha_{\text{el}}\,\sigma_{\text{el}} + \alpha_{\text{inel}}\,\sigma_{\text{inel}}}{\sigma_{\text{el}} + \sigma_{\text{inel}}}, \tag{5.4}$$

where σ_{el} and σ_{inel} is the cross sections for the elastic and inelastic processes, respectively.

The background fraction analysis shows a clear distinction between elastic and inelastic contributions. For the elastic component (case 1), only about 0.3% of events correspond to background, mainly

due to secondary interactions or misidentified tracks. The inelastic component (case 2) has a higher background fraction of roughly 2.3%, while case 3 and case 4 contribute around 0.16% and 0.06%, respectively. The overall background fraction for the reconstructed antiproton sample is approximately 3.3%. The signal purity remains high, confirming the robustness of the reconstruction and selection criteria.

Figure 5.1 shows the distribution of the difference between reconstructed and generated Z-positions of primary vertices in MC simulations. This distribution provides a quantitative measure of the vertex reconstruction accuracy.

By fitting the distribution with a Gaussian function, the mean value was determined to be 0.0609 ± 0.0005, indicating a small systematic shift between the reconstructed and true vertex positions. The standard deviation, $\sigma = 0.4898 \pm 0.0005$, represents the spatial resolution along the beam axis. The narrow width of the distribution confirms the high precision of the reconstruction algorithm, reproducing the true vertex positions with sub-millimeter accuracy. This strong correlation between the low vertex resolution and background fraction for case 3 and 4 demonstrates that precise vertex reconstruction effectively suppresses contamination in the reconstructed MC sample.

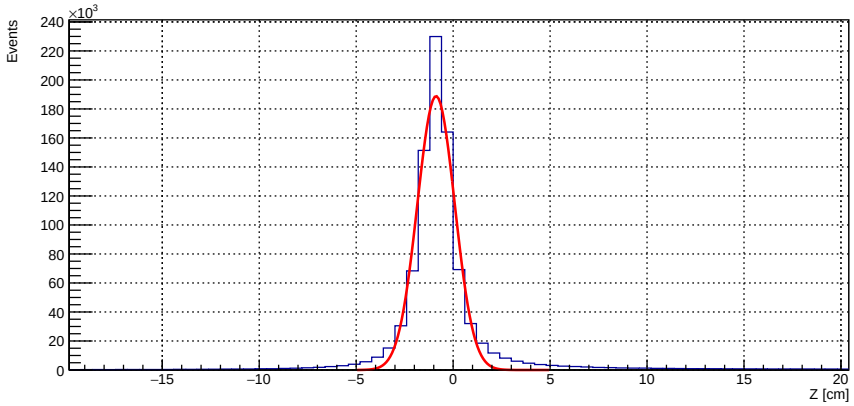

Figure 5.1: Distribution of the difference between reconstructed and generated Z-positions of primary vertices in Monte Carlo simulation.

Conclusion

This study presents a detailed estimation of the RICH detector efficiency and background for antiproton production measurements in the AMBER experiment. The RICH demonstrated excellent PID performance, and simulation was significantly improved by correcting the refractive index. The total background contamination was found to be 3.3%, confirming the robustness of the analysis. These results provide a solid foundation for precise antiproton cross-section measurements, crucial for interpreting cosmic-ray data and probing dark matter signals.

Acknowledgements

I would like to sincerely thank my professor, Dr. Andrei Gridin, for his guidance and support throughout this project. I am also very grateful to JINR for giving me this opportunity, and to the START team for their continuous support along the way.

References

[1] M. Aguilar, et al. (AMS collaboration), The Alpha Magnetic Spectrometer (AMS) on the international space station: Part II — Results from the first seven years, Phys. Rep. 894 (2021) 1–116. doi:10.1016/j.physrep.2020.09.003.

[2] Y. Akaike, et al. (CALET collaboration), The Calorimetric Electron Telescope on the International Space Station: Results from the first eight years on orbit, Adv. in Space Res. 74 (2024) 4353–4367. doi:10.1016/j.asr.2024.04.035.

[3] J. Chang, et al. (DAMPE collaboration), The DArk Matter Particle Explorer mission, Astropart. Phys. 95 (2017) 6–24. doi:10.1016/j.astropartphys.2017.08.005.

[4] G. H. Choi, et al. (ISS-CREAM collaboration), Measurement of High-energy Cosmic-Ray Proton Spectrum from the ISS-CREAM Experiment, ApJ 940 (2022) 107. doi:10.3847/1538-4357/ac9d2c.

[5] O. Adriani, et al. (PAMELA collaboration), Ten years of PAMELA in space, Nuovo Cimento Rivista 40 (2017) 473–522. doi:10.1393/ncr/i2017-10140-x.

[6] M. Boudaud, Y. Génolini, L. Derome, J. Lavalle, D. Maurin, P. Salati, P. D. Serpico, AMS-02 antiprotons' consistency with a secondary astrophysical origin, Phys. Rev. Res. 2 (2020) 023022. doi:10.1103/PhysRevResearch.2.023022. arXiv:1906.07119

[7] Precision cross-sections for advancing cosmic-ray physics. Input to the 2026 ESPPU from the XSCRC community

[8] S. Gabici et al., The origin of Galactic cosmic rays: Challenges to the standard paradigm, International Journal of Modern Physics D 28 (2019) 1930022. doi:10.1142/S0218271819300222.

[9] W. Baade and F. Zwicky, Remarks on Super-Novae and Cosmic Rays, Phys. Rev. 46 (1934) 76–77. doi:10.1103/PhysRev.46.76.2.

[10] Davide Giordano, Antiproton production measurement for indirect Dark Matter search at the AMBER experiment at CERN. 20.500.14242/199422

[11] P. D. Group et al., Review of Particle Physics, Progress of Theoretical and Experimental Physics 2020 (2020) 083C01. ISSN 2050-3911. doi:10.1093/ptep/ptaa104.